Design a Catalytic Cathode Material with Abundant Oxygen Vacancies to Accelerate the Kinetics of Lean-Electrolyte Lithium-Sulfur Batteries

Limin Mao,[a] Hongtao Xie,[a] Fei Wang,[a] and Jian Mao*[a]

Lean-electrolyte lithium-sulfur (Li–S) batteries are confronted with sluggish reaction kinetics, which required high catalytic materials to improve electrochemical performance. Herein, high catalytic-activity Ce-doped TiO_2 nanoparticles were combined into reduced graphene oxides (rGO) as the sulfur cathode (Ce-doped TiO_2/rGO/S). The impact of doping amounts of Ce on oxygen vacancies (OVs) was studied. Among the different Ce doping amounts, the 0.4 wt% Ce doping TiO_2 (0.4 Ce–TiO_2) exhibits the best catalysis and adsorption for Li_2S_6 due to the most OVs in 0.4 Ce–TiO_2. Rich OVs can provide more active sites for sulfur adsorption and present stronger catalytic activity to polysulfides. With an electrolyte to sulfur (E/S) ratio of $7 \, \mu L \, mg_S^{-1}$, the 0.4 Ce–TiO_2/rGO/S exhibits the best electrochemical capability when compared with TiO_2/rGO/S and rGO/S. It has a high capacity of $1421.9 \, mAh \, g^{-1}$ at 0.1 C ($1 \, C = 1675 \, mA \, g^{-1}$), and excellent rate performance. The 0.4 Ce–TiO_2/rGO/S also has a higher capacity and more stable cyclic performance than TiO_2/rGO/S when the temperature elevates to 60 °C.

1. Introduction

Electric vehicles and intermittent renewable energy such as wind and solar energy are both in sore need of advanced battery systems.[1] The lithium-sulfur (Li–S) battery, one of the most promising rechargeable batteries, draw great attention due to the high theoretical specific capacity ($1675 \, mAh \, g^{-1}$) and energy density ($2600 \, Wh \, kg^{-1}$), the low toxicity and cost of sulfur, so it's expected to achieve driving an electric vehicle 500 km.[1–3] However, the shuttle effect of polysulfides and sluggish reaction kinetics of polysulfides transferring to Li_2S_2/Li_2S hinder the commercial application of Li–S batteries. Besides, the amount of electrolyte is a very important parameter, which is evaluated by the ratio of electrolyte to sulfur (E/S). High E/S ratios can increase the discharge capacity and cycling performance of Li–S batteries.[4] However, the excessive electrolyte will reduce the energy density of Li–S batteries.[5] Universally, when the E/S ratio is over $10 \, \mu L \, mg_S^{-1}$, the electrolyte is up to more than 50 wt% of the whole cell.[6] So the lean-electrolyte Li–S batteries with high discharge capacity and stable cycles are pursued. Nevertheless, lean electrolyte slows down the kinetic reaction,[7] so high catalytic cathode materials are needed to fasten the kinetics.

As the most common catalyst, TiO_2 has been utilized as cathode hosts[8,9] and separators or interlayers[10,11] in Li–S batteries. TiO_2 with different morphology (yolk-shell S–TiO_2 nanoarchitecture,[9] multi-shelled structural TiO_{2-x}[12]) and its composites (such as TiO_{2-x} nanosheets with carbon nanotubes[13]) can efficiently absorb polysulfides and catalyze polysulfides to Li_2S_2/Li_2S.[14] The adsorption restrains the shuttle effect, and the catalysis expedites the kinetic reaction. Particularly, the rich oxygen vacancies (OVs) in TiO_2[13] can supply high activated trapping sites for adsorbing and catalyzing polysulfides and also narrow the bandgap of TiO_2 for rapid charge transfer.[15] Research also had proved that cation doping in TiO_{2-x} can improve the adsorption and catalytic activity for polysulfides.[16]

Herein, we fabricated the anatase TiO_2 doping by Ce element (Ce-doped TiO_2) to induce oxygen vacancies,[17] increasing the catalytic activity of TiO_2.[18,19] The Ce-doped TiO_2 was served as a strong absorbent and catalyst, and the reduced graphene oxide (rGO) was combined to provide a conductive network and a high specific area for hosting sulfur. We call the above composite cathode Ce-doped TiO_2/rGO/S, and it is the first TiO_2 as sulfur host for lean-electrolyte Li–S batteries at ambient and elevated temperatures.

2. Results and Discussion

2.1. Characterization of Samples

The TiO_2 with different Ce doping amounts (0.2, 0.4, 0.8 and 1.2 wt% Ce, noted 0.2, 0.4, 0.8 and 1.2 Ce–TiO_2, respectively) was synthesized by impregnation method. The Ce doping amounts are detected by the Inductively coupled plasma optical emission spectrometer (ICP-OES), and the results show the Ce amount is 0.19, 0.34, 0.73, and 1.12 wt% for 0.2, 0.4, 0.8, and 1.2 Ce–TiO_2, respectively, which has few deviations from our theoretical proportions. The successful Ce inducing is also

[a] L. Mao, H. Xie, F. Wang, Prof. J. Mao
Sichuan University
College of Materials science and engineering
No.24 South Section 1, Yihuan Road, Chengdu, 610065, China
E-mail: maojian@scu.edu.cn

proved by energy dispersive spectroscopy (EDS) of Ce-TiO$_2$ in Figure S1.

The O 1s spectra are tested to characterize the elemental composition and chemical state of the Ce-doped TiO$_2$ and TiO$_2$ (Figure 1a–e). The peaks at approximately 530.0 and 531.8 eV are attributed to the lattice oxygen (O$_L$) and oxygen vacancies (O$_v$), respectively.[20] The peak of O$_L$ is ascribed to the Ti–O–Ti. The content of O$_v$ increases with the increase of Ce content. The intensity of O$_v$ peak of Ce-doped TiO$_2$ (from 17.52% to ~19%) has an obvious increase than that of TiO$_2$ (12.1%), which demonstrated the abundant OVs in Ce-doped TiO$_2$, due to the Ce doping can promote the formation of OVs.[18] It can be explained as follows: the Ce 3d spectrum (Figure S2) of different Ce-doped TiO$_2$ presents four peaks at 905.19 and 886.29, 901.31 and 882.41, assigned to the Ce^{4+} 3d$_{3/2}$ and Ce^{4+} 3d$_{5/2}$, Ce^{3+} 3d$_{3/2}$ and Ce^{3+} 3d$_{5/2}$, respectively; the more Ce^{3+} in the high Ce content ($\geq$ 0.4 wt%) samples (Figure S2b–d) avails to the formation of more OVs because the oxygen vacancies mainly result from the decomposed of Ce^{4+}, based on the Equation (1):[21]

$$4CeO_2 \rightarrow 2Ce_2O_3 + 2\,OV + O_2 \uparrow . \tag{1}$$
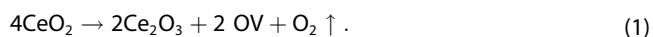
However, the OVs concentration of 0.4–1.2 Ce–TiO$_2$ is almost the same which may be owing to the superfluous Ce atoms aggregate to form atomic clusters rather than inducing more OVs. All samples are anatase phase TiO$_2$ (JCPDS card 21-1272) without other phases as the X-ray diffraction (XRD) pattern shows (Figure S3a). As Figure 3(b) shows, the Ce-doped TiO$_2$ has a sight offset to a lower angle, which results from the larger atomic radius of the Ce element than the one of the Ti element.[22]

The defect concentration of Ce-doped TiO$_2$ and TiO$_2$ was characterized by the Electron paramagnetic resonance (EPR). As Figure 1(f) showing, the Ce-doped TiO$_2$ exhibits a sharp peak ($g = 1.999$), where TiO$_2$ has only a little swell, which indicates Ce-doped TiO$_2$ has a higher concentration of defects than TiO$_2$. Meanwhile, the Ce-doped TiO$_2$ with a higher Ce doping amount has stronger EPR intensity. However, the X-ray photoelectron spectroscopy (XPS) (Figure 1c–e) shows the nearly consistent OVs concentration of 0.4–1.2 Ce–TiO$_2$. The higher EPR intensity of the higher Ce doping amount may result from the unsaturated electron pairs of more Ce atoms, not only from OVs.

The samples were composited with reduced graphene oxides (rGO) to as sulfur host (named TiO$_2$/rGO/S etc.). The Brunauer-Emmett-Teller (BET) specific surface area of rGO attain 52.7 m^{2}g^{-1} as the isothermal adsorption shown in Figure S4(a). The rGO has a wide pore size distribution (Figure S4b), ranging from 200–400 nm. The XRD results (Figure S3c) of Ce-doped TiO$_2$/rGO/S samples show that all samples were successfully loaded with sulfur (JCPDS card 08-0247). Comparing the XRD patterns of 0.4 Ce–TiO$_2$/rGO/S and rGO/S in Figure S3(d), the peaks of TiO$_2$ can be indexed in the pattern of 0.4 Ce–TiO$_2$/rGO/S.

The Scanning electron microscope (SEM) image (Figure S5a) of Ce-doped TiO$_2$/rGO/S shows that it has a three-dimensional (3D) network with many holes, and lots of particles disperse on the surface of rGO in the enlarged SEM image of Ce-doped TiO$_2$/rGO/S (Figure 2a). The SEM image of rGO/S (Figure S5b) also exhibits a porous structure. As shown in Figure 2(b), the EDS mappings of C, S, Ti, and O elements in the Ce-doped TiO$_2$/rGO/S substantiate the observed particles in Figure 2(a) are Ce-doped TiO$_2$, and the sulfur is evenly distributed. The sulfur
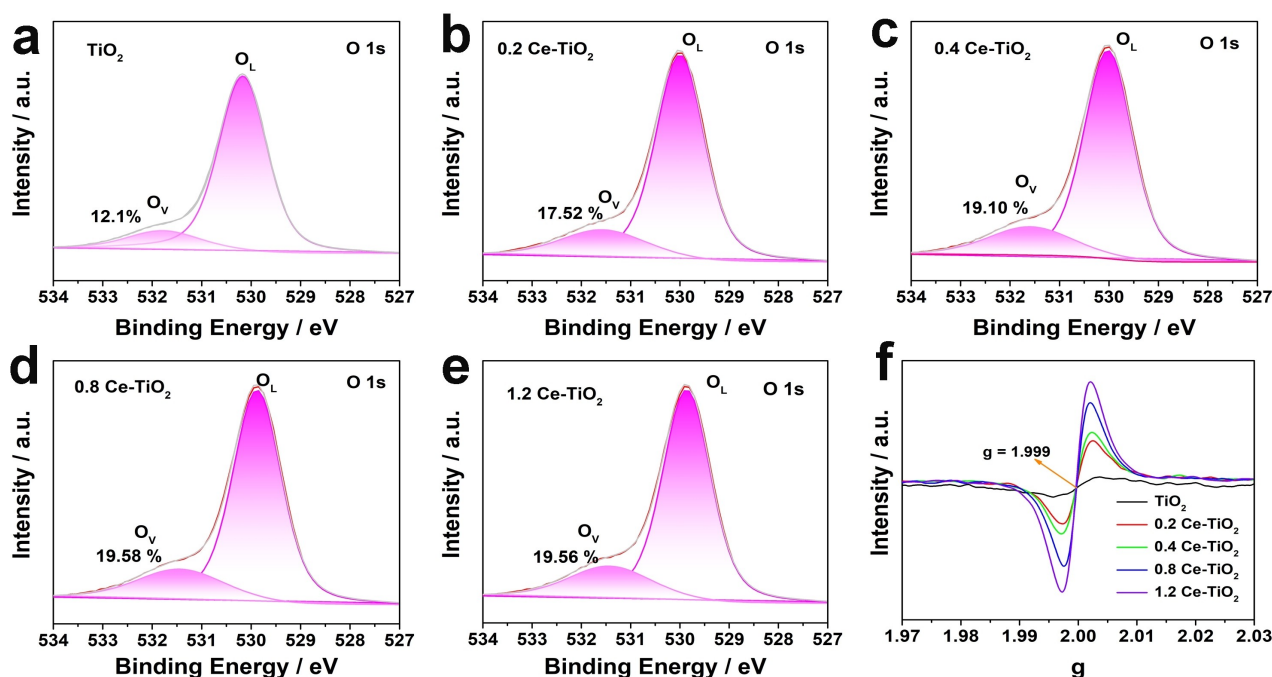

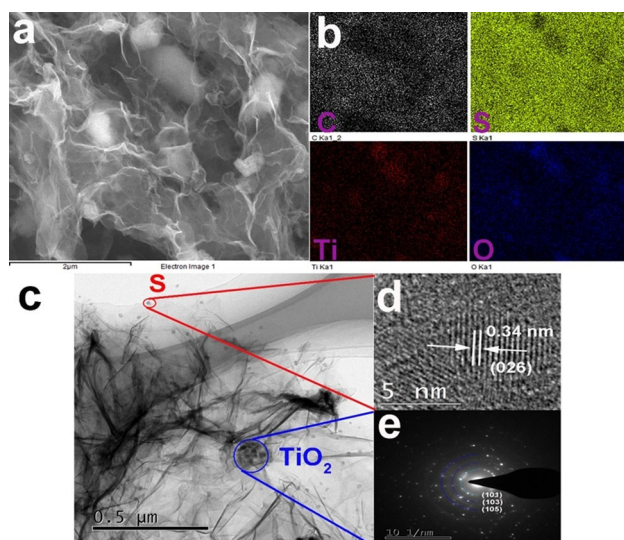**Figure 1.** a–e) O 1s spectra and f) EPR curves of TiO$_2$ and TiO$_2$ with different Ce doping.

Figure 2. a) SEM image and b) the corresponding EDS mapping of Ce-doped TiO_2/rGO/S. c) TEM image of Ce-doped TiO_2/rGO/S. d) HR-TEM image of the sulfur particle. e) SAED image of the Ce-doped TiO_2 particles.

particles and Ce-doped TiO_2 particles are also found in the Transmission electron microscope (TEM) image of Ce-doped TiO_2/rGO/S (Figure 2c). The high-resolution TEM (HR-TEM) image of the nanoparticle (Figure 2d) presents an interplanar distance of 0.34 nm, assigned to the (026) crystal surface of sulfur. The selected area electron diffraction (SAED) image in

Figure 2(e) shows the polycrystalline ring of anatase TiO_2. The TEM images of 0.4 Ce-doped TiO_2 and TiO_2 (Figure S6) show both have the same crystal plane spacing of 0.35 nm corresponding to the (101) plane of anatase TiO_2. The sulfur content of Ce-doped TiO_2/rGO/S, TiO_2/rGO/S, and rGO/S is estimated to be approximately 73 wt%, 74 wt%, and 72.5 wt%, respectively, by the Thermogravimetry (TG) curves (Figure S7).

2.2. Performance at Ambient Temperature

The adsorption testing of Li_2S_6 is carried out to verify the adsorption for Li_2S_6 by Ce-doped TiO_2 and TiO_2. In contrast to the blank Li_2S_6 sample, the color of solvents after being treated by Ce-doped TiO_2 and TiO_2 has visible fading (Figure 3 a inset), showing the polysulfides have been absorbed by Ce-doped TiO_2 and TiO_2. The 0.4 Ce–TiO_2 has the lightest color after absorbing Li_2S_6, while the 0.8 and 1.2 Ce–TiO_2 have a little more yellow than 0.4 Ce-doped TiO_2, which indicates the 0.4 Ce–TiO_2 has the strongest adsorption for polysulfides. The intensity change of characteristic peaks at 400–500 nm ascribed to the Li_2S_6[23] in the ultraviolet-visible (UV-Vis) curves (Figure 3a) also proves this.

The cyclic voltammetry (CV) curves of symmetric cells with and without Li_2S_6 of Ce-doped TiO_2/rGO, TiO_2/rGO, and rGO are tested to verify the liquid redox reaction and the results are shown in Figures 3b and S8. The CV curves with Li_2S_6 are much larger than the ones without Li_2S_6, indicating the cells without
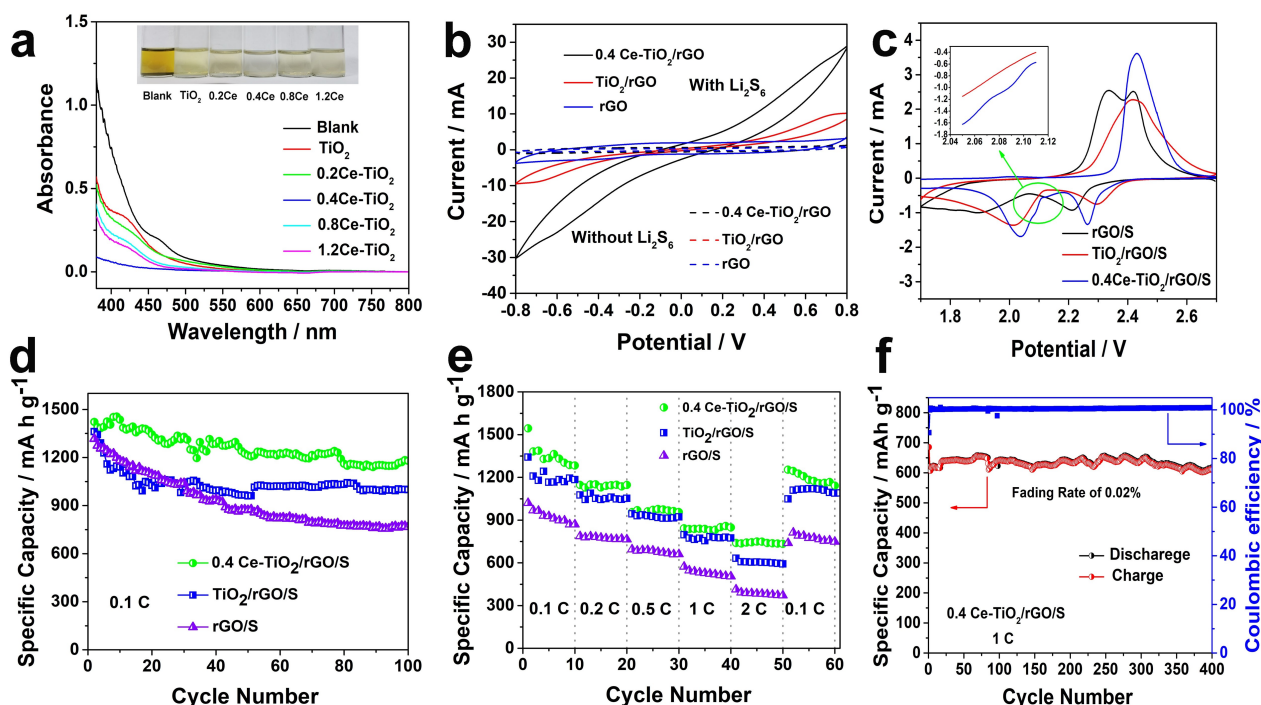

Figure 3. a) UV-Vis spectrum and the photograph of the Li_2S_6 solution with and without treating by Ce-doped TiO_2 or TiO_2. b) CV curves of the symmetric cells based on Ce-doped TiO_2/rGO, TiO_2/rGO, and rGO with and without Li_2S_6. c) CV curves and d) cycle performance of the cells with 0.4 Ce–TiO_2/rGO/S, TiO_2/rGO/S and rGO/S at 0.1 C. e) Rate performance of 0.4 Ce–TiO_2/rGO/S, TiO_2/rGO/S and rGO/S. f) Long-cycle performance at 1 C of 0.4 Ce–TiO_2/rGO/S. The E/S ratio is 7 μL mg$_S^{-1}$ in all cells.

Li_2S_6 manifest simple capacitive behavior, while CV curves with Li_2S_6 represent the samples that have catalysis for polysulfides.[24] From Figure 3(b), the rGO with feeble catalysis for Li_2S_6 is found by the CV curve of the cell-based rGO with Li_2S_6 only a little larger than the one without Li_2S_6. The curves of Ce-doped TiO_2 exhibit higher current density than TiO_2, manifesting the better catalytic activity of Ce-doped TiO_2. Based on Figure S8, the 0.2 Ce–TiO_2 is the worst catalyzer among the four Ce-doped TiO_2, while the 0.4 Ce–TiO_2 represents the best catalysis for Li_2S_6 among the Ce–TiO_2 systems. The catalytic activity is related to the concentration of OVs because the OVs as point defects can result in more sites for sulfur adsorption[25] and the OVs can promote the rupture of S–S bonding to expedite the reaction kinetics.[26] As shown in Figure 1, when the Ce content is greater than 0.4 wt%, the concentration of OVs doesn't increase with Ce increasing. The redundant Ce atoms may tend to aggregate, which may influence the catalytic effect of Ce-doped TiO_2. Therefore, the 0.4 Ce–TiO_2 is the best one as a catalyst for polysulfides, and it was chosen to investigate the effect of OVs on the lean-electrolyte Li–S batteries at ambiance and elevated temperature.

The CV curves (Figure 3c) of 0.4 Ce–TiO_2/rGO/S, TiO_2/rGO/S, and rGO/S were measured to certify the catalytic activity of samples. The 0.4 Ce–TiO_2/rGO/S shows the sharpest redox peaks than TiO_2/rGO/S and rGO/S, which indicates that the 0.4 Ce–TiO_2/rGO/S accelerates the reaction of polysulfides, due to the more OVs in 0.4 Ce–TiO_2/rGO/S. Based on the CV curves, the lower Tafel slope (Figure S9) of 0.4 Ce–TiO_2/rGO/S than TiO_2/rGO/S also proved the higher electrocatalytic effect.[27] So the more OVs can enhance the catalysis of TiO_2 for polysulfides.

The typical charge-discharge curves of different cathodes at 0.1 C (1 C = 1675 mA g^{-1}) are shown in Figure S10. The two platforms of the discharge curve correspond to the transformation of sulfur to polysulfides and the polysulfides to Li_2S_2/Li_2S, at ~2.3 and 2.1 V, respectively. The two platforms of 0.4 Ce–TiO_2/rGO/S are both longer than those of TiO_2/rGO/S and rGO/S, which profits from that the 0.4 Ce–TiO_2 adsorbs polysulfides vigorously and catalyzes the polysulfides to Li_2S_2/Li_2S rapidly. The cycle performance at 0.1 C of different cathodes is presented in Figure 3(d). The cells of 0.4 Ce–TiO_2/rGO/S, TiO_2/rGO/S, and rGO/S exhibit an initial specific discharge capacity of 1421.9, 1361.9, and 1316.5 mAh g^{-1}, respectively. After 100 cycles, the 0.4 Ce–TiO_2/rGO/S, TiO_2/rGO/S and rGO/S maintain a capacity fading of 0.17%, 0.26% and 0.41%, respectively. The 0.4 Ce–TiO_2/rGO/S quite performs good performance among the recent materials for Li–S batteries under lean electrolyte as shown in Table S1.

Figure 3e shows the rate cycles of 0.4 Ce–TiO_2/rGO/S, TiO_2/rGO/S, and rGO/S. The discharge specific capacity of 0.4 Ce–TiO_2/rGO/S is 1544.4, 1146.9, 956.1, 842.1 and 739.7 mAh g^{-1} at the current density of 0.1, 0.2, 0.5, 1 and 2 C, respectively. The discharge specific capacities of TiO_2/rGO/S and rGO/S are all lower than 0.4 Ce–TiO_2/rGO/S. When the current density recovers to 0.1 C, the discharge specific capacity of 0.4 Ce–TiO_2/rGO/S, TiO_2/rGO/S, and rGO/S are 1253.8, 1048.2, and 820.9 mAh g^{-1}, respectively. The galvanostatic charge-discharge curves of 0.4 Ce–TiO_2/rGO/S at different rates indicate the

complete profiles at 2 C (Figure S11). Distinctly, the 0.4 Ce–TiO_2/rGO/S cathode presents the highest-degree reversible redox reaction. The better performance of the 0.4 Ce–TiO_2/rGO/S cathode can be explained by the abundant OVs of 0.4 Ce–TiO_2. The OVs can enhance adsorption to polysulfides and quickened transformation between polysulfides to Li_2S_2/Li_2S.

The electrochemical impedance spectroscopy (EIS) (Figure S12a) exhibits a typical semicircle at high frequency and a slash at low frequency, corresponding to the charge transfer resistance (R_{ct}) and Warburg impedance (W), respectively.[28] The equivalent circuit is shown in Figure S12(b). The R_{ct} of 0.4 Ce–TiO_2/rGO/S is 69.4 Ω, lower than that of TiO_2/rGO/S (106.4 Ω), so the 0.4 Ce–TiO_2/rGO/S has a faster charge transfer than TiO_2. It may stem from the OVs in 0.4 Ce–TiO_2 that could narrow the bandgap, promoting the charge transfer.[15] The cycle performance of 0.4 Ce–TiO_2/rGO/S at 1 C is also tested under lean electrolyte. As Figure 3(f) shows, the 0.4 Ce–TiO_2/rGO/S still exhibits a high capacity and stable cycle. After 400 cycles, the specific capacity only has 0.02% fading. Comparing with the cycle performance of 0.4 Ce–TiO_2/rGO/S cathodes with higher E/S = 20, 15 μL mg$_s^{-1}$ at 1 C (Figure S13), the results of 0.4 Ce–TiO_2/rGO/S cathodes at E/S = 7 μL mg$_s^{-1}$ indicate the 0.4 Ce–TiO_2 indeed overcame the slow kinetics of lean electrolyte. According to the above results, the 0.4 Ce–TiO_2/rGO/S cathodes with rich oxygen vacancies all exhibit the optimal electrochemical performance among the three systems.

2.3. Electrochemical Performance at Elevated Temperatures

Research shows Ce–TiO_2 maintains distinguished catalysis at high temperatures,[16] so the catalysis of 0.4 Ce–TiO_2 for polysulfides at elevated temperatures is investigated by the symmetric cells of Li_2S_6 as Figure S14 shows. For all temperatures, the CV curves of the cells without Li_2S_6 exhibit capacitive behavior, however, the ones with Li_2S_6 exhibit a much higher current density, manifesting the 0.4 Ce–TiO_2/rGO and TiO_2/rGO can provide effective catalysis for Li_2S_6 at elevated temperatures. Moreover, the current density keeps increasing with the temperature rising, indicating that higher temperatures can more effectively enhance the catalytic activity for Li_2S_6. The CV curves of the cells based on 0.4 Ce–TiO_2/rGO and TiO_2/rGO are compared in Figure 4(a). The current densities of 0.4 Ce–TiO_2/rGO are all higher than the ones of TiO_2/rGO at each temperature, demonstrating the 0.4 Ce–TiO_2/rGO possesses stronger catalytic activity for Li_2S_6 than TiO_2/rGO.

Figure 4(b) is the EIS of 0.4 Ce–TiO_2/rGO/S cathodes at 25, 45, 60, and 90 °C. The R_{ct} decreases with the increase of operating temperatures. It can be ascribed that the higher temperature can improve the ionic conductivity and promote the infiltration of the electrolyte to the electrodes.[29]

The CV curves of 0.4 Ce–TiO_2/rGO/S at different temperatures are shown in Figure 4(c). The process of short-chain polysulfides reversing to S coincides at the oxidation peaks of approximately 2.4 V. As the temperatures increase, the CV curves exhibit more sharp peaks, demonstrating the elevated temperatures can facilitate redox kinetics. The oxidation peak
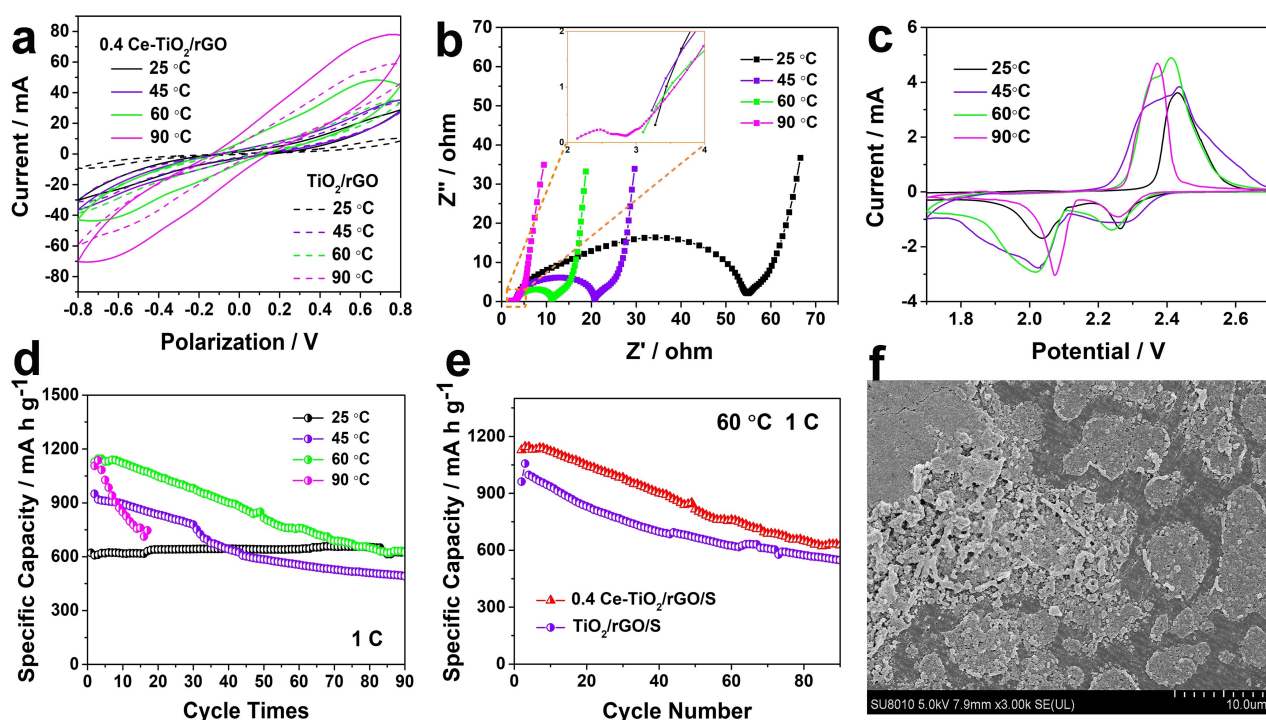
Figure 4. a) CV curves of the symmetric batteries based on 0.4 Ce–TiO$_2$/rGO and TiO$_2$/rGO. b) EIS spectrum, c) CV curves, and d) cycle performance of the cell with 0.4 Ce–TiO$_2$/rGO/S operating at 25, 45, 60, and 90 °C. e) Cycle performance of the cell with 0.4 Ce–TiO$_2$/rGO/S and TiO$_2$/rGO/S operating at 60 °C at 1 C. f) SEM image of the disassembled cell after shorting out at 90 °C.

at approximately 2.4 V shifts to lower potential with the increase of temperature, manifesting there is smaller polarization at higher temperatures. The cycle performance of the cells with 0.4 Ce–TiO$_2$/rGO/S at different temperatures at 1C is shown in Figure 4(d). The cells deliveries an initial specific capacity of 891.5, 950.1, 1128.2, and 1106.3 mAh g^{-1} at 25, 45, 60, and 90 °C, respectively. The increase of temperature can enhance the initial specific capacity, due to the faster charge transfer and higher catalytic activity. Nevertheless, the elevated temperatures also fasten the shuttle of polysulfides, so the cell operating at 45 °C has poorer cyclic performance than 25 °C. At 60 °C, the cell exhibits the best electrochemical performance compared with 45 and 90 °C. The cell operating at 60 and 90 °C shorts out after about 90 and less 20 cycles, respectively. The cycle performance of 0.4 Ce–TiO$_2$/rGO/S and TiO$_2$/rGO/S cathodes at 60 °C at 1 C is shown in Figure 4(e). The 0.4 Ce–TiO$_2$/rGO/S also has a better cycle performance.

The reason for the cell shorting out is investigated by disassembling the cell shorting out at 90 °C. The photograph of the Li anode and separator (Figure S15a) shows the separator has obvious melt and sticks with Li metal tightly. The SEM image of the side facing the lithium of the separator (Figure 4f) shows lots of particles deposited on the separator, blocking the almost pores in the separator. The XRD pattern of the separator of the disassembled cell (Figure S15b) demonstrates the particles are mainly composed of Li$_2$CO$_3$ (JCPDS card 72-1216). The form of Li$_2$CO$_3$ particles may be due to the side reaction of Li metal with electrolyte. The SEM images of the side facing the lithium of separator of disassembled cells operating at 25, 45, 60, and 90 °C (Figure S16) manifest the higher temperatures can promote the formation of more Li$_2$CO$_3$ particles. The melt of the separator and the severe side reaction both may cause the shorting out.

From the above mentioned, elevated temperatures are conducive to realizing a high initial specific capacity through enhancing the charge transfer, catalysis of Ce-doped TiO$_2$ (or TiO$_2$), and so on. Nevertheless, elevated temperatures also accelerate the polysulfides shuttling and make more serious side reactions between Li metal and electrolyte, even the separator melts, which can cause the cell to short out. For all that, the 0.4 Ce–TiO$_2$/rGO/S cathode delivers better electrochemical performance than TiO$_2$/rGO/S by the high catalytic activity of 0.4 Ce–TiO$_2$.

3. Conclusions

The TiO$_2$ doping different Ce amount as adsorbent for lean-electrolyte Li–S batteries was studied firstly. The higher Ce doping amount caused more OVs, which enhance the catalysis of TiO$_2$ for polysulfides. The fewer OVs in 0.2 Ce–TiO$_2$ cause the worse adsorption and catalysis. The 0.4 Ce–TiO$_2$ delivered the best adsorption and catalysis for polysulfides. With lean electrolyte (E/S = 7 μL mg$_s^{-1}$), the 0.4 Ce–TiO$_2$/rGO/S exhibited the highest electrochemical performance among the TiO$_2$/rGO/S and rGO/S, such as an initial specific capacity of 1421.9 mAh g^{-1} at 0.1C and excellent rate performance, a specific capacity of 739.7 mAh g^{-1} at 2C. The long-cycle performance at 1 C of 0.4

Ce−TiO$_2$/rGO/S also is a stable cycle. The high electrochemical performance of Ce-doped TiO$_2$/rGO/S derives from that the rich OVs facilitate Ce-doped TiO$_2$ absorbing and catalyzing polysulfides vigorously.

The electrochemical performance of as-prepared cells at 60°C is better than that operating at 45 and 90°C. The 0.4 Ce−TiO$_2$/rGO/S with high catalytic activity delivers more outstanding electrochemical performance. At 60°C, the 0.4 Ce−TiO$_2$/rGO/S presents an initial specific capacity of 1128.2 mAh g^{-1} at 1 C and better cycle performance than TiO$_2$/rGO/S.

Experimental Section

Preparation of the Ce-doped TiO$_2$

Ce-doped TiO$_2$ is prepared by the simple and common impregnation method.[30] Nano-sized anatase TiO$_2$ and ceric sulfate (Ce$_2$(SO$_4$)$_3$, 99%, Kelong, China) were dispersed into the distilled water with ultrasonic treatment, followed the stirring 3 h at 40°C. After 3 times of filtration and washing, the powder was dried at 60°C. The Ce-doped TiO$_2$ was obtained by calcining the above powder at 600°C for 4 h in the air. The different mass ratios of Ce (0.2, 0.4, 0.8, and 1.2 wt%) are prepared to analyze the effect of doping amounts on electrochemical performance, noted 0.2, 0.4, 0.8, and 1.2 Ce−TiO$_2$, respectively.

Preparation of Ce-doped TiO$_2$/rGO/S, TiO$_2$/rGO/S, and rGO/S

The ultrafine sulfur is loaded in the surface of GO, based on the following chemical reaction:

$$S_2O_3{}^{2-} + 2H^+ \rightarrow S \downarrow + H_2O + SO_2 \uparrow .$$
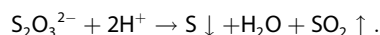
A specific process is the following: The graphene oxide (GO) slurry (1 wt%, purchased from Deyang Carbonene, China) was dispersed into the sodium thiosulfate (Na$_2$S$_2$O$_3$, 99%, Kelong, China) solution. 0.1 mol L^{-1} H$_2$SO$_4$ solution was added dropwise into the above mixture under magnetic stirring. After the reaction was complete, the supernate was poured, and distilled water was added to wash the mixture several times. Finally, the dispersion of GO loading sulfur (GO/S) was gained. The Ce-doped TiO$_2$ and excess ascorbic acid (as a reductant for GO) were added into the above-dispersed solution (GO/S), and the mixture was sonicated for 20 min. The mixture was reacted at 80°C for 2 h to reduce the GO to reduced GO (rGO) and finally got rGO/S gel, meanwhile, the Ce-doped TiO$_2$ particles (with different doping amounts) were loaded into the rGO/S gel. After washing several times and freeze drying, the Ce-doped TiO$_2$/rGO/S was obtained. For uniform distribution of sulfur, the Ce-doped TiO$_2$/rGO/S was heated at 155°C for 12 h in the argon atmosphere. The TiO$_2$/rGO/S and rGO/S were synthesized with the same process as contrasts.

Polysulfides adsorption testing

Li$_2$S$_6$ solution (3 mmol L^{-1}) was prepared by dissolving sulfur and lithium sulfide (Li$_2$S) with a molar ratio of 5:1 into dimethoxyethane (DME) in an argon-filled glovebox, stirring at 60°C for 48 h.[23] 20 mg Ce-doped TiO$_2$ and TiO$_2$ were added into 2 mL Li$_2$S$_6$ solution, respectively, followed by stewing for 24 h.

Symmetric cell assembly and measurements

Li$_2$S$_6$|Li$_2$S$_6$ symmetric cells were assembled as 2032 type coin cells in an argon-filled glovebox. Firstly, Ce-doped TiO$_2$/rGO aerogel was obtained by adding Ce-doped TiO$_2$ into the mixture solution of GO and excess ascorbic acid with sonicating for 20 min. The mixture was heated at 80°C for 2 h, followed by freeze drying. The TiO$_2$/rGO and rGO aerogel were fabricated with the same method. Ce-doped TiO$_2$/rGO (or TiO$_2$/rGO or rGO) and polyvinylidene fluoride (PVDF) were dispersed at a mass ratio of 9:1 into N-methyl-2-pyrrolidone (NMP), then the slurry was loaded on carbon paper as the cathodes and anodes simultaneously. Li$_2$S$_6$ solution (0.5 M) was prepared by dissolving the sulfur and Li$_2$S at a molar ratio of 5:1 into the electrolyte of 1 M bis(trifluoromethane) lithium salt (LiTFSI) and lithium nitrate (LiNO$_3$, 2 wt%) dissolving in 1,3-dioxolane (DOL) and DME (1:1 by volume). And 40 μL Li$_2$S$_6$ solution was added into symmetric cells. The CV test of the Li$_2$S$_6$|Li$_2$S$_6$ symmetric cells was performed at the scan rate of 50 mV s^{-1} at the potential range of −0.8 to 0.8 V.[31]

Electrochemical measurements

The Ce-doped TiO$_2$/rGO/S, Ketjen black, and PVDF were ground with the mass ratio of 8:1:1, and the NMP was a solvent. The powders were mixed as slurry and coated on the carbon paper (14.2 mm in diameter), followed by the vacuum dried at 60°C for 12 h. The areal sulfur loadings were ranged at 1.6–2.4 mg cm^{-2}. The lithium metal as anode, the 2032 type coin cell was assembled in an argon-filled glovebox with the Celgard 2500 as separators. The used electrolyte is composed of 1 M LiTFSI and 2 wt% LiNO$_3$ dissolving in DOL and DME (1:1 by volume). The E/S ratio is 7 μL mg$_S$$^{-1}$. Electrochemical impedance spectroscopy (EIS) and cyclic voltammetry (CV) measurements were performed at the CHI660E electrochemical workstation. The EIS was tested at a frequency range of 0.1 Hz–1000 kHz and the CV curves were obtained at a voltage window of 1.7–2.7 V vs. Li$^+$/Li with a scan rate of 0.1 mV s^{-1}. The charge-discharge performance was collected using the Neware galvanostatic charge-discharge instrument (CT-4008T-5V10Ma-164) between 1.7–2.7 V vs. Li$^+$/Li. Applied currents and specific capacities were calculated based on the mass ratio of sulfur in the cathodes.

Characterization

Inductively coupled plasma optical emission spectrometer (ICP-OES, Agilent 5110, China) was utilized to detect the amount of Ce doping. X-ray diffraction (XRD) patterns of samples were tested using a polycrystalline X-ray diffractometer (Shimadzu 6100, Japan; Cu K_α radiation: $\lambda = 0.154184$ nm) with the sweep rate of 5° min^{-1}. The scanning electron microscopy (SEM, Hitachi SU8010, Japan) and transmission electron microscopy (TEM, JEOL JEM-2100F, Japan) were utilized to characterize the morphology of the samples. The concentration of oxygen vacancies was characterized by Electron paramagnetic resonance (EPR, EMXmicro-6/1/P/L, Karlsruhe, Germany). X-ray photoelectron spectroscopy (XPS) spectra were obtained on Kratos XSAM 800 (UK). The sulfur content of Ce-doped TiO$_2$/rGO/S (TiO$_2$/rGO/S or rGO/S) was measured by the thermos-gravimetry analyses (TGA) on a DTG-60 (Japan) from room temperature to 600°C with a heating rate of 10°C min^{-1} in an N$_2$ atmosphere. UV-Vis spectrometer (UV-1700, Shimadzu, Japan) was used to measure the concentration of Li$_2$S$_6$ solutions exposed to different adsorbents. The specific surface area and pore size distribution of samples are determined by the nitrogen adsorption (Autosorb iQ, Contador, the USA).

Conflict of Interest

The authors declare no conflict of interest.

[1] Z. Sun, J. Zhang, L. Yin, G. Hu, R. Fang, H.-M. Cheng, F. Li, *Nat. Commun.* **2017**, *8*, 14627.

[2] X. Liang, Y. Liu, Z. Wen, L. Huang, X. Wang, H. Zhang, *J. Power Sources* **2011**, *196*, 6951–6955.

[3] G. Liu, K. Feng, H. Cui, J. Li, Y. Liu, M. Wang, *Chem. Eng. J.* **2020**, *381*, 122652.

[4] S. Thieme, J. Brückner, A. Meier, I. Bauer, K. Gruber, J. Kaspar, A. Helmer, H. Althues, M. Schmuck, S. Kaskel, *J. Mater. Chem. A* **2015**, *3*, 3808–3820.

[5] R. Fang, S. Zhao, Z. Sun, D. W. Wang, H. M. Cheng, F. Li, *Adv. Mater.* **2017**, *29*, 1606823.

[6] M. Zhao, B. Q. Li, H. J. Peng, H. Yuan, J. Y. Wei, J. Q. Huang, *Angew. Chem. Int. Ed.* **2020**, *59*, 12636–12652; *Angew. Chem.* **2020**, *132*, 12736–12753.

[7] S. C. Nagpure, T. R. Tanim, E. J. Dufek, V. V. Viswanathan, A. J. Crawford, S. M. Wood, J. Xiao, C. C. Dickerson, B. Liaw, *J. Power Sources* **2018**, *407*, 53–62.

[8] X. T. Gao, Y. Xie, X. D. Zhu, K. N. Sun, X. M. Xie, Y. T. Liu, J. Y. Yu, B. Ding, *Small* **2018**, *14*, e1802443.

[9] Z. W. Seh, W. Li, J. J. Cha, G. Zheng, Y. Yang, M. T. McDowell, P. C. Hsu, Y. Cui, *Nat. Commun.* **2013**, *4*, 1331.

[10] Z. Xiao, Z. Yang, L. Wang, H. Nie, M. Zhong, Q. Lai, X. Xu, L. Zhang, S. Huang, *Adv. Mater.* **2015**, *27*, 2891–8.

[11] O. Eroglu, M. S. Kiai, H. Kizil, *J. Alloys Compd.* **2020**, *838*, 155607.

[12] E. H. M. Salhabi, J. Zhao, J. Wang, M. Yang, B. Wang, D. Wang, *Angew. Chem. Int. Ed.* **2019**, *58*, 9078–9082; *Angew. Chem.* **2019**, *131*, 9176–9180.

[13] Y. Wang, R. Zhang, J. Chen, H. Wu, S. Lu, K. Wang, H. Li, C. J. Harris, K. Xi, R. V. Kumar, S. Ding, *Adv. Energy Mater.* **2019**, *9*, 1900953.

[14] M. Wang, Y. Song, N. Wei, Y. Shao, G. Sheng, J. Sun, *Chem. Eng. J.* **2021**, *418*, 129407.

[15] D. R. Deng, F. Xue, C. D. Bai, J. Lei, R. Yuan, M. S. Zheng, Q. F. Dong, *ACS Nano* **2018**, *12*, 11120–11129.

[16] Z. Shi, M. Li, J. Sun, Z. Chen, *Adv. Energy Mater.* **2021**, *11*, 2100332.

[17] A. R. Albuquerque, A. Bruix, I. M. G. Dos Santos, J. R. Sambrano, F. Illas, *J. Phys. Chem. C* **2014**, *118*, 9677–9689.

[18] H. Wang, X. Chen, S. Gao, Z. Wu, Y. Liu, X. Weng, *Catal. Sci. Technol.* **2013**, *3*, 715–722.

[19] X. Fan, J. Wan, E. Liu, L. Sun, Y. Hu, H. Li, X. Hu, J. Fan, *Ceram. Int.* **2015**, *41*, 5107–5116.

[20] Z. Li, C. Zhou, J. Hua, X. Hong, C. Sun, H. W. Li, X. Xu, L. Mai, *Adv. Mater.* **2020**, *32*, e1907444.

[21] D. Maarisetty, S. S. Baral, *Ceram. Int.* **2019**, *45*, 22253–22263.

[22] J. Xie, D. Jiang, M. Chen, D. Li, J. Zhu, X. Lü, C. Yan, *Colloids Surf. A* **2010**, *372*, 107–114.

[23] T. Lei, W. Chen, J. Huang, C. Yan, H. Sun, C. Wang, W. Zhang, Y. Li, J. Xiong, *Adv. Energy Mater.* **2017**, *7*, 1601843.

[24] B. Yu, Y. Chen, Z. Wang, D. Chen, X. Wang, W. Zhang, J. He, W. He, *J. Power Sources* **2020**, *447*, 227364.

[25] H. C. Wang, C. Y. Fan, Y. P. Zheng, X. H. Zhang, W. H. Li, S. Y. Liu, H. Z. Sun, J. P. Zhang, L. N. Sun, X. L. Wu, *Chem. Eur. J.* **2017**, *23*, 9666–9673.

[26] J. Wang, L. Jia, H. Liu, C. Wang, J. Zhong, Q. Xiao, J. Yang, S. Duan, K. Feng, N. Liu, W. Duan, H. Lin, Y. Zhang, *ACS Appl. Mater. Interfaces* **2020**, *12*, 12727–12735.

[27] Z. Shi, Z. Sun, J. Cai, X. Yang, C. Wei, M. Wang, Y. Ding, J. Sun, *Adv. Mater.* **2021**, *33*, e2103050.

[28] F. Wang, Z. Hu, L. Mao, J. Mao, *J. Power Sources* **2020**, *450*, 227692.

[29] Y. Kim, D.-J. Jang, *RSC Adv.* **2013**, *3*, 16945.

[30] Slamet, H. W. Nasution, E. Purnama, S. Kosela, J. Gunlazuardi, *Catal. Commun.* **2005**, *6*, 313–319.

[31] J. Jin, W. Cai, J. Cai, Y. Shao, Y. Song, Z. Xia, Q. Zhang, J. Sun, *J. Mater. Chem. A* **2020**, *8*, 3027–3034.